Stretchable multichannel antennas in soft wireless optoelectronic implants for optogenetics

Sung Il Park[a,b,c], Gunchul Shin[b,c], Jordan G. McCall[d,e], Ream Al-Hasani[d,e], Aaron Norris[f], Li Xia[g], Daniel S. Brenner[d,e], Kyung Nim Noh[b,c], Sang Yun Bang[b,c], Dionnet L. Bhatti[d,e], Kyung-In Jang[b,c], Seung-Kyun Kang[b,c], Aaron D. Mickle[d,e], Gregory Dussor[h], Theodore J. Price[h], Robert W. Gereau IV[d,e,i], Michael R. Bruchas[d,e,f,i,1], and John A. Rogers[b,c,1]

[a]Department of Electrical and Computer Engineering, Texas A&M University, College Station, TX 77843; [b]Department of Materials Science and Engineering, Beckman Institute for Advanced Science and Technology, University of Illinois at Urbana–Champaign, Urbana, IL 61801; [c]Frederick Seitz Materials Research Laboratory, University of Illinois at Urbana–Champaign, Urbana, IL 61801; [d]Washington University Pain Center, Washington University School of Medicine, St. Louis, MO 63130; [e]Department of Anesthesiology, Washington University School of Medicine, St. Louis, MO 63130; [f]Department of Anesthesiology, Washington University School of Medicine, St. Louis, MO 63130; [g]Biomedical Engineering, Washington University School of Medicine, St. Louis, MO 63130; [h]School of Behavioral and Brain Sciences, The University of Texas at Dallas, Richardson, TX 75080; and [i]Department of Neuroscience, Washington University School of Medicine, St. Louis, MO 63110

Optogenetic methods to modulate cells and signaling pathways via targeted expression and activation of light-sensitive proteins have greatly accelerated the process of mapping complex neural circuits and defining their roles in physiological and pathological contexts. Recently demonstrated technologies based on injectable, microscale inorganic light-emitting diodes (μ-ILEDs) with wireless control and power delivery strategies offer important functionality in such experiments, by eliminating the external tethers associated with traditional fiber optic approaches. Existing wireless μ-ILED embodiments allow, however, illumination only at a single targeted region of the brain with a single optical wavelength and over spatial ranges of operation that are constrained by the radio frequency power transmission hardware. Here we report stretchable, multiresonance antennas and battery-free schemes for multichannel wireless operation of independently addressable, multicolor μ-ILEDs with fully implantable, miniaturized platforms. This advance, as demonstrated through in vitro and in vivo studies using thin, mechanically soft systems that separately control as many as three different μ-ILEDs, relies on specially designed stretchable antennas in which parallel capacitive coupling circuits yield several independent, well-separated operating frequencies, as verified through experimental and modeling results. When used in combination with active motion-tracking antenna arrays, these devices enable multichannel optogenetic research on complex behavioral responses in groups of animals over large areas at low levels of radio frequency power (<1 W). Studies of the regions of the brain that are involved in sleep arousal (locus coeruleus) and preference/aversion (nucleus accumbens) demonstrate the unique capabilities of these technologies.

wireless optogenetics | stretchable electronics | wireless power transmission | deep brain stimulation | antenna

O ptogenetics exploits a toolbox of light-sensitive proteins for optical manipulation of neural networks as a powerful means for the study of circuit-level mechanisms that underlie psychiatric diseases (1–4). Canonical optogenetic experiments in the brain require cranial insertion of an optical fiber to illuminate a region of interest (5, 6). Although this approach permits simple behavior modeling, constraints in animal motion and alterations in natural behaviors due to fiber tethering and external fixation complicate use in chronic longitudinal models and in experiments that assess complex responses. Many of these limitations can be bypassed with optoelectronic technologies and wireless receivers, as recently demonstrated in optogenetic stimulation of the brain, the peripheral nerves, and the spinal cord (4, 7–13). Systems that offer soft, compliant mechanical properties and thin, fully implantable designs are particularly advantageous (7). These systems, however, have still not been optimized to fully take advantage of the power of combining

mouse genetics/optogenetics with long-term behavioral manipulation or with multicolor stimulation capacity. Another limitation of current systems is their inability to wirelessly stimulate multiple circuits simultaneously by using different channels with multiple wavelengths of light. Such capabilities would enable interrogation of complex circuit behaviors in awake animals, a major goal of modern neuroscience research. To address these key shortcomings in existing technology, we report a class of multicolor, long-term–implantable, radio-controlled devices that enable advanced modes of operation in behavioral studies of awake, freely moving mice.

The work involves three key advances: (*i*) devices with designs for use in the deep brain, with examples in optogenetic control of sleep/wake transitions via stimulation of the locus coeruleus (LC) (14); (*ii*) motion tracking systems for coordinated control over multiple transmission antennas, to allow ultralow power radio frequency operation over large areas; and most importantly, (*iii*) specialized radio frequency antennas and associated circuits for independent control over multiple light sources in a single platform, with examples in optogenetic modulation of aversion/preference behaviors via dynorphinergic neurons in nucleus accumbens shell (NAcSh) using two-channel wireless devices for stimulation of separate regions of the brain individually,

---

Significance

Soft, multichannel antennas enable wireless, battery-free operation of fully implantable optoelectronic systems designed for use in studies of brain function. These systems support independent, remote control of multiple light-emitting diodes that inject into targeted regions of the deep brain, where they separately stimulate activity in genetically and spatially discrete neural circuits, via the use of the techniques of optogenetics. These capabilities represent significant advancements over alternative technology approaches for this important branch of neuroscience research. In vivo studies using optimized systems demonstrate wireless control of two different brain regions and distinct activation of subpopulations of neurons using separately activated light sources associated with these subdermal devices.

---

in a single mouse. This experimental demonstration is significant because, although activation of the dorsal and ventral regions of the NAcSh are known to generate preference and aversion behaviors, respectively, no other approaches can stimulate both regions in the same animal simultaneously. The results reported here illustrate this possibility in awake, behaving animals using a wireless, completely subdermal power and control system. The ability for independent, wireless power delivery and control over multiple light sources with emission wavelengths across the visible range also suggests related opportunities in optogenetic stimulation and inhibition. Such capabilities can be achieved by combining devices described here with recently developed light-sensitive proteins for advanced types of in vivo optogenetics and behavioral experiments (3).

Results

Optoelectronic Design. The device platform enables separate, wireless operation of a collection of injectable microscale inorganic light-emitting diodes (μ-ILEDs, based on unpackaged devices with dimensions of 220 μm width, 270 μm length, and 50 μm thickness) in designs that are also adaptable to other light-delivery platforms. A radio frequency energy harvester receives signals from a transmitter, rectifies them, and triples the resulting voltage to provide a direct-current output for the μ-ILEDs. An impedance matching circuit, designed to maximize the received power, uses a ceramic chip capacitor (3 pF; 0.20 mm width, 0.4 mm length, 0.22 mm thickness) and an inductor (2.7 nH; 0.20 mm width, 0.4 mm length, 0.22 mm thickness) connected in series. The rectifier incorporates miniaturized Schottky diodes (1.7 mm width, 1.5 mm length, 0.5 mm thickness) and

ceramic chip capacitors (5 pF; 0.20 mm width, 0.4 mm length, 0.22 mm thickness). The multiplier involves three Schottky diodes, identical to those in the rectifier, for the purpose of boosting the voltages provided by the rectifier (~0.9 V) to values sufficient to operate the μ-ILEDs (~2.7 V). To accommodate anatomical shapes and natural motions inside the targeted biological environment, the devices exploit principles of stretchable electronics in the form of serpentine metal interconnects passivated by layers of polyimide (40 μm thickness), with the entire system encapsulated in a low modulus silicone elastomer (~0.5 MPa, 100 μm thickness for superstrate and substrate) to yield soft mechanics at the system level (effective modulus, ~1.7 MPa) (Fig. 1A) (7). The fabrication procedures, along with details of the components and the circuit layouts, appear in *Methods* and *SI Appendix*, Fig. S1 and Table S1.

The thin, miniaturized geometry (4.3 mm width, 8 mm length, and 0.7 mm thickness); ultra-lightweight construction (33 mg); and mechanical compliance of these devices facilitate full implantation and chronic use in the brain (Fig. 1B). The system includes two parts: a back-end power harvesting and control unit and an injectable needle-shaped substrate that allows delivery of the μ-ILEDs (Fig. 1C, *Right Top* and *Right Bottom*) to targeted structures in the deep brain. Both components offer soft mechanics to impose minimal constraints on natural motions of the surrounding tissue (Fig. 1 C, *Left* and D), with reliable operation under levels of deformation that significantly exceed those expected in freely moving animals (7). Accelerated testing indicates that the soft silicone encapsulation preserves device functionality for 6 d when immersed in PBS (7.4 pH) at 90 °C, and the devices show no degradation after more than 2 mo in similar
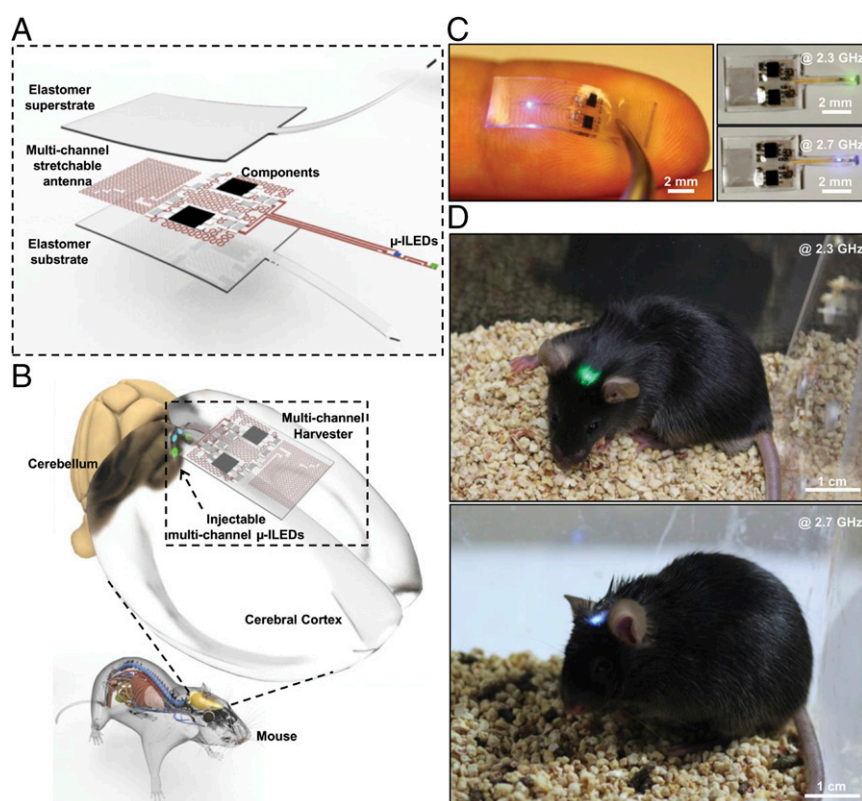
Fig. 1. Multichannel, soft wireless optoelectronic systems for optogenetics. (A) Exploded-view schematic illustration of the multichannel energy harvester components of the system. (B) Schematic illustration of the anatomy and location of the device relative to the brain. (C) Pictures of a two-channel operating device on a fingertip, deformed by application of localized force with a pair of tweezers to illustrate the soft mechanics (*Left*) and wireless operation in the air (*Right Top* and *Right Bottom*). This harvester activates a green μ-ILED at 2.3 GHz (channel 1, right to the top) and a blue μ-ILED at 2.7 GHz (channel 2, right to the bottom). (D) Images of mice implanted with the two-channel optoelectronic system, operating at a frequency of 2.3 (*Top*) and 2.7 (*Bottom*) GHz, respectively.

solution at 37 °C (*SI Appendix*, Fig. S2). Arrhenius-based extrapolations of testing at 60 °C and 90 °C suggest lifetimes of ~6 mo at 37 °C (*SI Appendix*, Note S1) (15). These soft, flexible components also reduce brain trauma upon insertion and minimize tissue damage after chronic implantation and activation (9, 10, 16). The high degree of compliance of the injectable part of the system can, however, confound mechanical penetration into the brain tissue. Previous approaches exploit releasable injection needles to overcome this challenge (9, 10). Here, a biodegradable needle made of poly–lactic-coglycolic acid (PLGA) obviates the need for extraction; this needle provides sufficient stiffness for injection into regions of the deep brain such as the LC and nucleus accumbens (NAc) but fully dissolves after exposure to biological fluids (*SI Appendix*, Fig. S3A) (17–19). In vitro testing shows that at 37 °C the needles lose half of their thickness (an eightfold reduction in their bending stiffness) in 3 d, with complete dissolution within a week (*SI Appendix*, Fig. S3 *B and C*). Heat generation is also a potential concern for long-term implantation and operation of electrical devices in animals. Experimental studies using implantable thermal sensors show that optical power densities of 10 mW/mm^2 (50% duty cycle; 10 Hz period; 50 ms pulse width) do not cause any significant, steady state temperature changes in the surrounding tissue (*SI Appendix*, Fig. S4). We note that the same concepts in multichannel antennas and wireless, battery-free operation can be applied to a broad range of other platforms for light delivery, including waveguide arrays and other technologies.

Optical and Electrical Characteristics.

The key feature of these devices is that they support multichannel operation, thereby overcoming a critical limitation of the single-channel, single-wavelength capabilities of previously reported wired and wireless systems (7–11, 13). Here, an advanced, stretchable antenna structure integrates multiple capacitive coupling traces to yield nonoverlapping resonances for frequency-selective harvesting and control. Each two-channel antenna consists of three serpentine lines (Fig. 2*A*, blue, red, and black line), where each pair (blue and red line, red and black line) involves resonant capacitive coupling with its neighbor. In particular, coupling between the blue and red traces (channel 1, Fig. 2*A*) and between the red and black traces (channel 2, Fig. 2*A*) enables operation at 2.3 (channel 1) and 2.7 (channel 2) GHz, respectively. To illustrate this operation, computations of electric field magnitudes near the surfaces of the serpentine traces at a frequency of 2.3 GHz reveal enhanced capacitive coupling (20), and therefore resonant operation, associated with channel 1 but not channel 2, as featured in black and red dotted boxes (Fig. 2*B*, *Right*). Such coupling can be captured by the reflection coefficient (S_{11}) for incident electromagnetic waves (7, 20). Reductions in S_{11} correspond to decreased reflections and therefore improved power transmission efficiencies. The results exhibit two separate resonances, corresponding to two independently addressable channels of operation (Fig. 2*C*). The circuit diagram in Fig. 2*D* highlights the nature of signal flows from the antenna to the corresponding DC voltage output nodes. Images of an operating device demonstrate that the frequency of the incident rf radiation can be adjusted to activate the channels independently

Fig. 2. Overview of electrical and optical characteristics of a two-channel stretchable antenna. (*A*) Schematic illustration of a two-channel stretchable antenna (*Left*) and magnified view of two input ports (*Right*). Here, serpentine lines are highlighted by colors (blue, red, and black), for purposes of clarity. Operation at channel 1 is associated with capacitive coupling between the blue and red lines; operation at channel 2 is related to the coupling between the red and black lines. (*B*) Normalized magnitude of the electric field on the serpentine lines (*Left*) at a frequency of 2.3 GHz. Magnified views, corresponding to the regions highlighted by the black and red dotted boxes, show capacitive coupling between adjacent serpentine lines (blue, red, and black). (*C*) Scattering parameters of the two-channel stretchable antenna. (*D*) Block diagram of the two-channel stretchable optoelectronic system. Channels 1 and 2 operate at frequencies of 2.3 and 2.7 GHz, respectively. (*E* and *F*) Measurements of the optical intensity generated in the nontargeted channel as a function of the optical intensity in the targeted channel at a frequency of 2.3 and 2.7 GHz, respectively. The dotted line identifies the threshold radio frequency power required to activate the nontargeted μ-ILED in each channel. (*G*) Maximum optical intensity at the targeted channel before the onset of the operation at the nontargeted channel as a function of channel separation. Here, an operation frequency at the targeted channel is 2.3 GHz, and operation frequencies at the nontargeted channels vary from 2.7 to 3.1 GHz.

([Movie S1](#)). The optical intensity generated in the nontargeted channel as a function of that in the targeted channel appears in Fig. 2 *E* and *F*. As indicated by the dotted lines, the intensity can reach ~12 mW/mm², which is more than sufficient to activate optogenetic proteins, before the onset of the operation in the nontargeted channel (21–23). The direct proximity of the light emitters in these injectable optoelectronic systems to the regions of interest in the brain enables activation of light-sensitive proteins with intensities of ~10 mW/mm², much lower than those needed at the light source regions of systems that require delivery of light via use of waveguides (~100 mW/mm²) (24). The designs of the stretchable antennas can be selected to achieve channel separations that can meet nearly any requirement in cross-coupling, as in *SI Appendix*, Note S2. Fig. 2*G* exhibits the maximum optical intensity at the targeted channel before the onset of the operation at the nontargeted channels as a function of channel separation from 0.4 to 0.8 GHz. Measurement results reveal that multichannel optoelectronic systems can drive optical intensities over 100 mW/mm², when the

channel separation is above 0.7 GHz. In this way, cross-coupling between channels can be designed to negligible levels.

Advanced versions of the antenna design in Fig. 2 can support independent manipulation of three separate channels. The scattering parameters of such an antenna that consists of four serpentine lines (Fig. 3*A*, red, black, blue, and green line) where each pair (red and black line, black and blue line, and blue and green line) exhibits capacitive coupling to its neighbor at a distinct frequency indicate operation at 2.3 (channel 1), 2.7 (channel 2), and 3.2 (channel 3) GHz. As before, computations of the electric field magnitude at 2.3 GHz illustrate selective capacitive coupling associated with the pair of traces that defines channel 1. These findings are confirmed through a set of measurements and images of the devices (Fig. 3 *C–G*). As with the two-channel system, there is no significant cross-coupling for the conditions of interest (Fig. 3 *D–F*). For both two- and three-channel systems, the angular variations in power received at each channel can affect operation (4, 7, 20). Calculations show that the radiation patterns associated with each
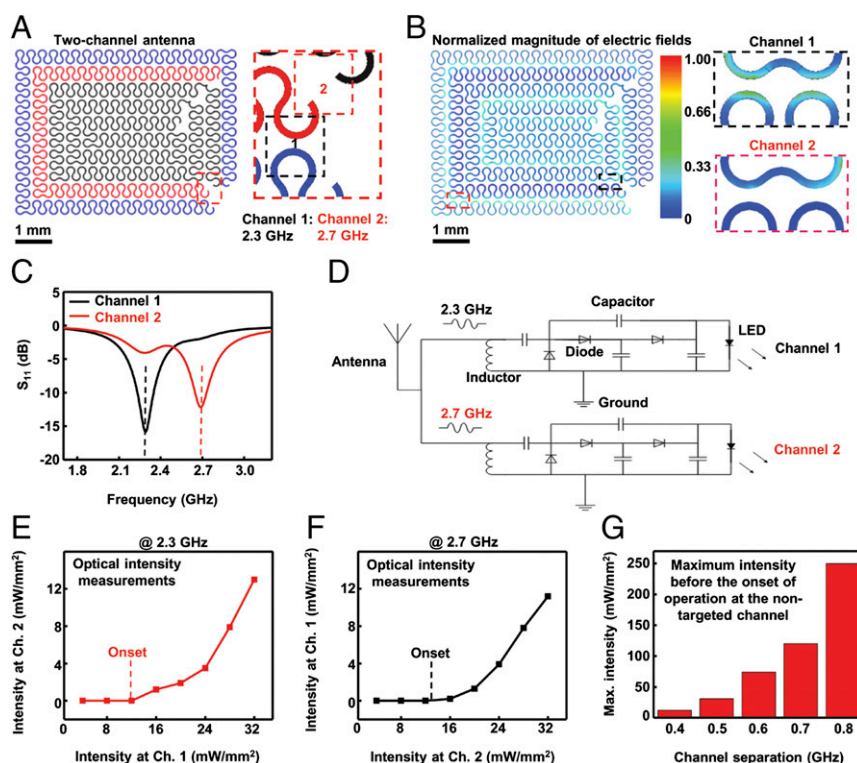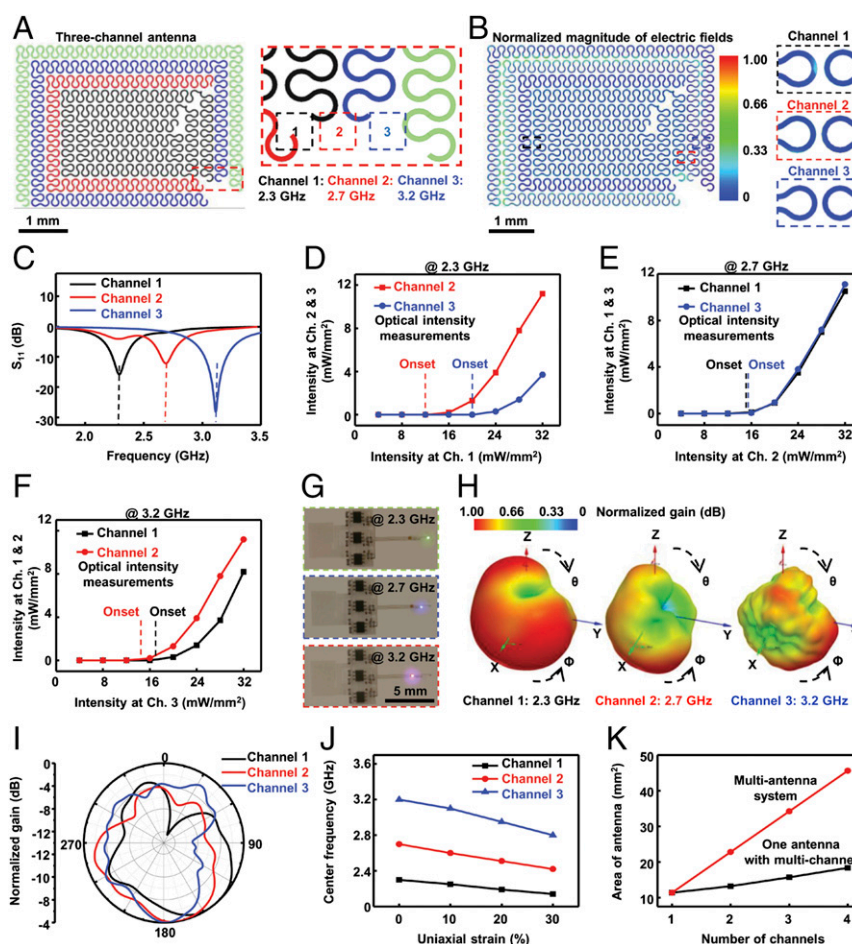

Fig. 3. Electrical characteristics of a three-channel stretchable antenna. (*A*) Schematic illustration of a three-channel stretchable antenna with a magnified view. The antenna consists of four serpentine lines (red, black, blue, and green). Here, the serpentine lines are highlighted by colors (red, black, blue, and green), for purposes of clarity. Channels 1, 2, and 3 are tuned at a frequency of 2.3, 2.7, and 3.2 GHz, respectively. Operation at channel 1 is associated with capacitive coupling between the red and black lines, operation at channel 2 is related to the coupling between the black and blue lines, and operation at channel 3 is connected with the coupling between the blue and green lines. (*B*) Normalized magnitude of the electric field on the serpentine lines at a frequency of 2.3 GHz. Enlarged views show capacitive coupling between adjacent serpentine lines. (*C*) Scattering parameters of the three-channel antenna. Each dotted line indicates the operating frequency of each channel. (*D–F*) Measurements of optical intensity generated in the nontargeted channels as a function of the optical intensity in the targeted channel at a frequency of 2.3 (*D*), 2.7 (*E*), and 3.2 (*F*) GHz, respectively. Dotted lines represent the threshold power required for activation of the nontargeted μ-ILEDs in each channel. Such results define a maximum single-channel activation threshold. (*G*) Images of wireless operation of the three-channel stretchable antenna at a frequency of 2.3 (*Top*; green), 2.7 (*Middle*; blue), and 3.2 GHz (*Bottom*; red), respectively. (*H*) Angular radiation patterns of the three-channel stretchable antenna at a frequency of 2.3 (*Left*), 2.7 (*Middle*), and 3.2 (*Right*) GHz, respectively. (*I*) Cross-sectional view of *H* at θ = 90°. (*J*) Variations of center frequencies as a function of strain applied at each channel. (*K*) Comparison of the area of one antenna with multichannel design to that of a multiantenna system.

channel, in all cases, are similar, ensuring that each receives (or transmits) an equivalent amount of power at a given orientation (Fig. 3 *H* and *I*). In addition, the serpentine layouts of the antennas and the soft, elastomeric substrate and superstrate afford linear elastic response to strain (7). Tensile strains lead to shifting of the resonant frequencies to lower values, as expected from previously reported single-channel antennas (Fig. 3*J*) (7). This three-channel example highlights clearly the dramatic reduction in overall size compared with an otherwise equivalent arrangement of three separate, single-channel antennas (Fig. 3*K*). Advanced impedance matching techniques allow for further minimization of cross-coupling, thereby extending the number of channels that can be independently operated (*SI Appendix*, Fig. S6) (20). A practical limit for operation in the low gigahertz frequency ranges (0.7~3.5 GHz, corresponding to a window of transparency for biological tissues) is ~eight channels, based on a frequency range/channel margin of 2.8/0.4 (25, 26).

Modeling of the Electromagnetic Properties of Stretchable Antennas with Serpentine Designs. Multichannel operation relies on the capacitive coupling that occurs between adjacent serpentine lines. This coupling can be captured analytically with solutions to the 2D Laplace equation (Fig. 4 and *SI Appendix*, Note S3) for simple antenna structures with serpentine geometries approximated by sinusoidal curves (Fig. 4 *A* and *B*). Here the electromagnetic interactions can be captured as a sum of infinitesimally small capacitors with gaps defined by the separation between adjacent lines (Fig. 4*B*). As the gap increases, the capacitive coupling decreases, with an analytical dependence that is consistent with numerical simulations (Fig. 4 *C*

and *D*). These studies reveal that the total capacitance of a stretchable antenna is approximately ~1.5 pF. To achieve resonance in the low GHz range, inductances of 2~3 nH are required, which is feasible within the dimensions of the antennas (20). Similar strategies can be extended to calculations of the inductances to yield the resonance frequencies. This analytical approach dramatically reduces the computational burden of full simulations of the actual antenna layouts by providing a starting point for the designs. Moreover, the results confirm that the operation of these types of antennas relies critically on capacitive effects.

The input impedance of the antenna is also important, as proper impedance matching can maximize the power transmission efficiency. The designs exploited here use an asymmetric geometry to increase the impedance over the very low values that are typically associated with antennas in this small size regime. Studies of input impedance as a function of the location of the input port provide insights into the role of this asymmetric geometry in input impedance and thus radiation efficiency. Moving the input from port 1 to port 4 breaks the symmetry, thereby increasing the impedance (Fig. 4 *E* and *F*) (20). Using these concepts to realize impedances of 50 ohms ensures maximum power transfer (20). The values of the reflection coefficient, S_{11}, are extremely sensitive to input impedance (Fig. 4*G*). The reflection values at each port, from 1 to 4, are 50%, 5%, 0.3%, and 25%, respectively (Fig. 4*H*).

Motion-Tracking Arrays of Transmission Antennas. Even with optimized impedance matching and antenna design, as the number of
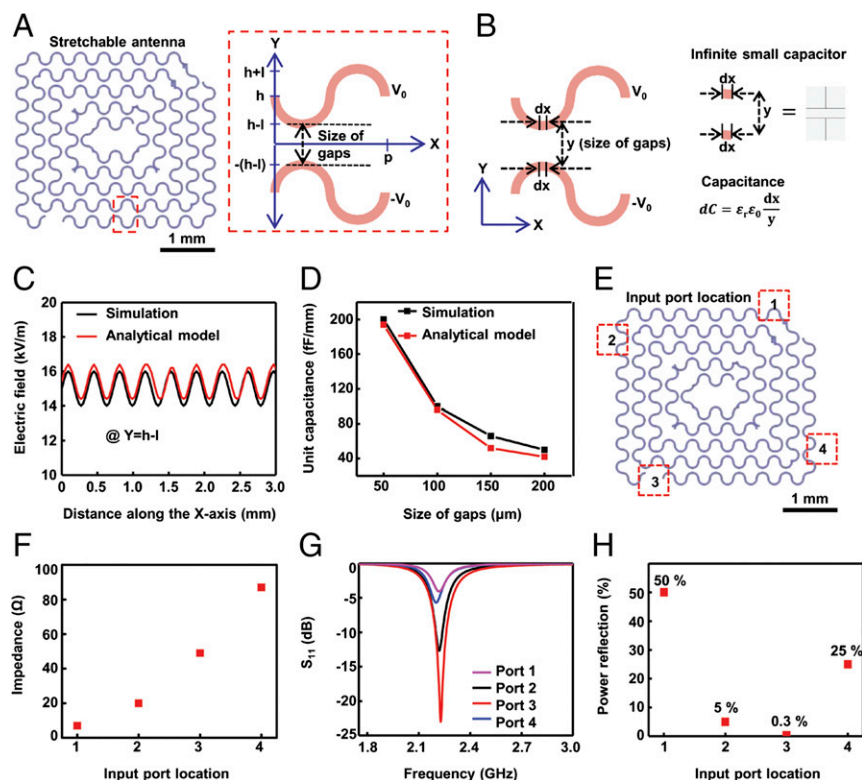

Fig. 4. Analytical modeling of the capacitive coupling and investigations of the input impedance as a function of input port location. (*A*) Schematic illustration of serpentine lines approximated with sinusoidal curves. The top (*Bottom*) line is biased at V_0 (–V_0). The red dotted line represents a unit cell of a pair of serpentine lines. (*B*) Equivalent circuit model where the serpentine lines are treated as a sum of infinitely small capacitors with top and bottom plate width of dx, separated by a gap of y. ε_r and ε_0 are relative permittivity and permittivity of the air, respectively. (*C*) Magnitude of electric fields (numerical simulations in black; analytical modeling in red) along the line (Y = h – l). Here, h = 500 μm and l = 380 μm. (*D*) Unit capacitance (numerical simulations in black; analytical modeling in red) as a function of gap between adjacent serpentine lines. (*E*) Schematic illustration of a stretchable antenna. Each number represents the location of an input port. (*F*) Impedance as a function of input port location. (*G*) Scattering coefficients, S_{11}, of a stretchable antenna at each port. (*H*) Power reflection as a function of input port. The results indicate the extent to which electromagnetic waves are reflected at each input port, where low values are highly desirable.

channels increases, corresponding increases in the total transmitted power could be necessary, depending on the nature of the optogenetic experiment. The upper limits could, with traditional systems, exceed exposure guidelines (25, 26). An actively managed array of antennas and a separately controlled transmission system that tracks the motions of the animals enable overall reductions in power by confining power delivery only to the relevant regions of an experimental assay chamber. Here, digital image processing on data collected with a monitoring camera (*SI Appendix*, Note S4 and Fig. S7A) locates the animal and then sends control signals to a multiplexer (MUX) that activates the antenna array in a way that directs power selectively to the corresponding area (*SI Appendix*, Fig. S7 B and C) (27). As such, transmission only occurs in the immediate environment of the targeted mouse, thereby greatly enhancing the efficiency of operation, to allow average power levels as low as 0.5 W (*SI Appendix*, Fig. S8) for a typical case (Movie S2). This type of selective activation also lends itself well to complex behavioral assays such as conditioned place preference or those that demand coverage over large areas, social interactions, home cage manipulations, or complex environments.

Wireless Optogenetic Activation of the LC Noradrenergic System in a Home Cage Arousal Paradigm. Multichannel operation that overcomes a critical limitation of the single-channel, single-wavelength capabilities introduced here demonstrates their utility for neural manipulation in native, homecage environments as well as standard behavioral assays with freely behaving mice. The LC has previously been implicated as a potent arousal center, such that activation of LC neurons can lead to sleep/wake transitions and speed emergence from anesthesia (28, 29). We set out to determine whether these subdermal devices can optogenetically drive naturalistic behaviors within the home cage by wireless photostimulation of LC-NEs. To do so, we used mice that express Cre recombinase under the promoter for galanin (Gal-Cre), which is expressed in a majority of noradrenergic LC neurons (LC-NEs) in combination with virally transduced Cre-dependent expression of ChR2 (14, 28–30). In these animals, the µ-ILED was placed directly adjacent to the LC to assess the ability of LC activation to drive locomotor activity during normal daily sleep periods in the mouse home cage (Fig. 5 A and B). Immunohistochemical analyses in Gal-Cre mice injected with AAV5–DIO–EF1α–ChR2 showed robust ChR2 expression (yellow) in the LC that overlaps with tyrosine hydroxylase (TH) expression (red), consistent with expression selectively in the galaninergic subset of LC-NE neurons (Fig. 5C) and previous studies (30). We singly housed Cre-expressing (Cre+) and Cre-negative (Cre–) littermates in home cages mounted on custom-built adapters that hold rf-emitting antennas in close proximity to the home cage (∼5 cm from the cage wall and floor) (*SI Appendix*, Fig. S7A and Fig. 5D). We followed a normal 12:12 h light:dark cycle and recorded video footage of the mice during a period of normal sleep and recorded for three successive 15-min periods. During the first and third periods, there was no activation of the implantable system (baseline and poststimulation), but during the second period, the implanted device was activated to drive LC neuronal activity by ChR2 (10 Hz, 50 ms pulse widths) (Fig. 5B) (14). Photostimulation of Galanin-expressing LC neurons drove increased locomotor activity in Cre+ animals compared with the pre- and postactivation period (Fig. 5E). In contrast, photostimulation of LC neurons in littermate Cre– mice

Fig. 5. Single-channel optogenetic studies in home cage behavioral responses. (A) Illustration of light illumination to LC in the mouse brain. (B) Experimental paradigm for testing optogenetic control of arousal. (C) Confocal micrograph of virally induced ChR2 expressions in galanin-expressing neurons in the LC region. TH immunoreactivity is red, and ChR2-eYFP native fluorescence is yellow. (D) Photograph of hardware setup, six-panel antennas line the bottom and side of the home cage. (E) Representative heat map of position in home cage during each epoch of the experiment for a Gal-Cre+ animal. Map is only plotted where the animal explored in the home cage (i.e., the animal was stationary in the baseline and poststimulation epochs) but freely explored during stimulation. (F) Analysis of the total distance traveled during each epoch in a home cage (n = 3–5 per group) (****P < 0.0001 two-way repeated-measures ANOVA with Bonferroni post hoc test).

did not alter the locomotor activity (Fig. 5F) (****$P < 0.0001$ two-way repeated-measures ANOVA with Bonferroni post hoc test). Taken together, these data demonstrate that selective photoactivation of galanergic LC neurons produces arousal and furthermore that these wireless devices can be easily used to perform behavioral experiments within the native home cage environment, which include studies of sleep or resting states that would otherwise be difficult with tethered cables.

Multichannel, Bidirectional Wireless Control of Reward and Aversion.

Wireless subdermal optogenetic probes that offer multichannel integration with discrete neuronal subpopulations are needed to extend our knowledge of complex neural circuitry in more ethologically, naturalistic environments and behaviors. For example, multichannel capabilities are valuable in the context of experiments where multiple neuronal subpopulations need to be independently engaged. Recent efforts have shown that photostimulation of dynorphinergic neurons in the NAcSh is sufficient to induce both aversive and preference behaviors (12). Photostimulation of dynorphinergic cells in the ventral NAcSh (vNAcSh) shell through activation of the kappa opioid receptor (KOR) elicits aversive behavior. Activation of nearby dorsal NAcSh (dNAcSh) dynorphin cells, however, in another KOR-mediated process elicits preference behavior. Characterization of nearby neuronal circuits previously required separate animals, with separate fiber optic implants within each subregion for optogenetic stimulation. The multichannel devices introduced here can define and modulate this spatially compact circuit with a single group of animals. Multichannel devices implanted in preprodynorphin–IRES–cre-positive mice that were infected with an AAV5–DIO–ChR2–eYFP virus to selectively express ChR2 in dynorphinergic neurons in the NAcSh demonstrate this capability (Fig. 6 A–C) (12). Here, the vNAcSh targets one μ-ILED (channel 1) and the nearby dNAcSh targets the other μ-ILED (channel 2), separated by a distance of 1 mm (Fig. 6A). A custom-made unbiased, balanced two-compartment conditioning apparatus ($52.5 \times 25.5 \times 25.5$ cm³; Fig. 6D) allows assessment of preference or aversion behavior by comparing the amount of time spent in the μ-ILED–on (rf-on) side to the time spent in the μ-ILED–off side. Isolated photostimulation of the vNAcSh through activation of channel 1 produces aversive behavior (Fig. 6 E and F, ventral and *SI Appendix,* Fig. S9), whereas in the same animal illumination of the dNAcSh through activation of channel 2 produces a real-time preference behavior (Fig. 6 E and F, dorsal, and *SI Appendix,* Fig. S9; one-way ANOVA Bonferroni post hoc; ****$P < 0.0001$ rf-off vs. vNAcSh and dNAcSh vs. vNAcSh and **$P < 0.01$ dNAcSh vs. both and vNAcSh vs. both). Here we show the subdermal multichannel operation can photostimulate two discrete subregions in the NAcSh in a single animal using a fully subdermal implantable tether-free mode. These devices expand the range of complexity for in vivo optogenetic experiments that can be performed and provide a flexible solution for multichannel functionality for neural circuit dissection.

Discussion

The development of soft, fully implanted devices with battery-free operation and independently controlled channels for multicolor illumination represents a significant technology advance for optogenetic studies. A key component of the hardware is a miniaturized multichannel antenna that harvests rf power through multiple, capacitive metallic traces, thereby providing nonoverlapping resonance frequencies. Although existing technologies can, in principle, provide operation over multiple light sources, they enable only single-wavelength illumination. When a rectifying circuit delivers DC output to light sources with different colors, electrically connected in parallel, those source with low turn-on voltages illuminate preferentially (20). Multiple, separate electrical systems with different resonance frequencies avoid this problem but are not well suited for levels of miniaturization needed for full implantation. The designs reported here overcome this limitation, for simultaneous, wireless control of multiple circuits, in wireless schemes that are compatible with animals in complex environments, including the potential for manipulation of social interactions.
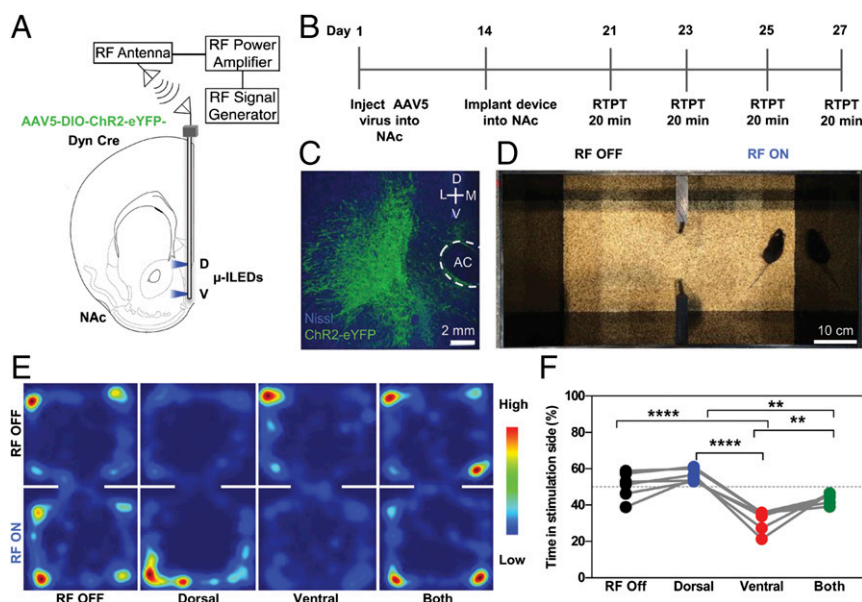

Fig. 6. Multichannel optogenetic activation of reward and aversion. (A) Cartoon of directionally controlled light spread of μ-ILED devices for isolating subregions of NAcSh. (B) Experimental paradigm for testing optogenetic control of reward and aversion. (C) Confocal micrograph of virally induced ChR2 expression in dynorphin-expressing neurons in the NAcSh. Nissl cell body stain is blue, and ChR2-eYFP native fluorescence is green. (D) Photo of the real-time place testing assay. (E) Representative heat map of time spent in the stimulation (rf-on) side following no stimulation, dorsal or ventral wireless photostimulation, and dorsal and ventral photostimulation together. (F) Stimulation with dorsal μ-ILED drives a real-time place preference, but stimulation with ventral μ-ILED drives an aversion, measured as a significant increase or decrease in time spent in the stimulation side (%), respectively. Stimulating both ventral and dorsal μ-ILEDs has no significant effect on behavior. Data are represented as mean ± SEM, n = 6. One-way ANOVA, Bonferroni post hoc; ****$P < 0.0001$ rf-off vs. ventral and dorsal vs. ventral; **$P < 0.01$ dorsal vs. both and ventral vs. both.

We provide evidence of simultaneous but separate optogenetic manipulation of multiple parts of the nervous system as an example of the possibilities for this device design. Our multichannel devices allow the direct interrogation of specific, discrete circuits within the brain in individual behaving animals at the same time. Importantly, we show that these devices are capable of differentially activating brain regions as close together as 1 mm. Given the small size of the mouse brain and the numerous examples of brain regions with closely neighboring neuronal populations providing disparate functions (as shown here in the NAcSh but also found in other brain regions such as the central vs. basolateral amygdala and the tightly packed hypothalamus), the ability to dissect circuit functions on a millimeter level can allow for the increased understanding of how these complicated circuits influence brain function. Studies to verify interactions between brain circuits have largely been assumed or inferred through anatomical, multielectrode array recording or fMRI studies that are limited in their ability to stimulate multiple areas or record activity simultaneously with behavior. This can now be achieved using these multichannel platforms to stimulate, inhibit, or modulate multiple circuits in the brain simultaneously while recording behavioral responses without the encumbrance of tethered wires. When combined with recently developed light-sensitive proteins for advanced types of in vivo optogenetics and behavioral experiments (3), such integration can provide clearer evidence for integrated function of targeted neural circuits in a host of animals via stimulation and/or inhibition of circuits or even signaling pathways (31).

Adaptive power delivery systems are essential in this context, not only for the practical use of such multichannel approaches in traditional experimental assays but also in long-range operation or multiplexed use across collections of animals, all with low-cost rf transmission hardware. Although the immediate benefits of these advances on behavioral experiments are clear, they also enable the development of additional useful features such as wirelessly powered, fully implantable rf-controlled optofluidic systems (32) and wireless closed-loop optogenetic devices where one channel controls data transmission and the other channel offers power management. Straightforward extensions of this platform will allow simultaneous closed-loop sensing modalities and electrical stimulation where each function is assigned to each channel and controlled independently.

Methods

Fabrication of Multichannel Devices. Fabrication was conducted on a clean glass slide (75 mm length, 50 mm width, and 1 mm thickness). Spin-casting polymethyl methacrylate (PMMA; 495 PMMA A8, Microchem) at $0.177 \times g$ for 30 s and curing at 70 °C for 6 h formed a coating with thickness of 200 nm. Subsequently, spin-casting a precursor to polydimethylsiloxane (PDMS; Sylgard 184) at 1,000 rpm for 30 s and curing at 70 °C for 6 h yielded an overcoat with a thickness of 100 μm. An 18 μm-thick copper foil (Dupont) laminated onto the PDMS, patterned by photolithography (AZ 5214E, AZ Electronic Materials) and copper etching, defined the antenna and interconnects. Small amounts of lead-free solder paste (SMD290SNL250T5, Chipquik) applied to the surface mount devices and the μ-ILEDs (Cree Inc.) and baked at 285 °C in a vacuum oven for 10 min bonded the components to the patterned interconnects. An epoxy adhesive (200 nm), cured at 20 °C for 5 min, bonded this platform to the needle. Spin-casting PDMS at 1,000 rpm for 30 s and curing at 70 °C for 6 h formed a final overcoat to complete the fabrication.

Fabrication of a Biodegradable Needle. Hot pressing the PLGA (65:35, Sigma-Aldrich Inc.) thin film at 100 °C for 5 min, followed by laser-cutting, formed thin PLGA (~75 μm thick) needle-shaped substrates.

Electromagnetic Simulations of Multichannel Stretchable Antennas. We used a commercially available finite element method tool, high frequency structural simulator (HFSS), to calculate the S_{11} values, the normalized electric field magnitudes, and angular radiation patterns with a mouse mesh model where layers corresponding to biological tissues are modeled as Cole-cole relaxation models (25). Simulations revealed the following parameter values: 4.84 dBd antenna gain, 97% antenna efficiency, 95% rectifying efficiency, and 30% led efficiency.

Measurements of Thermal Characteristics. We submerged multichannel optoelectronic systems in saline solution and monitored optical intensities as a function of time at various temperatures from 37 °C to 90 °C. Here, a hotplate was used to control the temperature of saline solution. For measurements of LED output, we used an optical measurement system (Extech LT300 Precision Digital Light Meter).

Measurements of Optical Intensities. We used an optical measurement system (Extech LT300 Precision Digital Light Meter) to measure output of the LEDs. For accurate measurements of each individual channel, we prepared three types of samples, each with a different color LED, to facilitate spectrally separate measurements of each channel.

Long-Term Implantation. Of 15 devices implanted for animal studies, all remained functional, without significant change in operation, for more than 2 mo. Movie S2 shows a representative device during operation.

Animals. Adult (25~35 g) male mice were group-housed, given access to food pellets and water ad libitum, and maintained on a 12:12-h light/dark cycle (lights on at 7:00 AM). The Animal Care and Use Committee of Washington University approved all procedures, which conformed to NIH guidelines.

Stereotaxic Surgery. For the arousal experiments, we used mice expressing Cre recombinase under the promoter for galanin (Gal-Cre) or littermate controls in combination with virally transduced Cre-dependent expression of ChR2 to target galaninergic neurons in the LC (33, 34). For surgery, we anesthetized the mice with isoflurane in an induction chamber and placed the animals in a stereotaxic frame that maintained anesthesia with 1~2% isoflurane through a nose cone. We injected AAV5–DIO–ChR2 unilaterally into the LC [coordinates from bregma: –5.45 anterior–posterior (AP), ±1.25 medial–lateral (ML), and –.00 mm dorsal–ventral (DV)] in mice (Cre+ or Cre–) (30). For multichannel control of neuronal subpopulations experiments, we injected AAV5–DIO–ChR2–eYFP into the dNAcSh of preprodynorphin–IRES–cre-positive mice with targets of stereotaxic coordinates from bregma (+1.30 AP, ±0.5 ML, –4.25 mm DV) or vNAcSh stereotaxic coordinates from bregma (+1.30 AP, ±0.5 ML, –4.75 mm DV) (12). A minimum of 2 wk after the viral injections, we stereotactically implanted the devices in mice using the same coordinates as above for AP and DV but at ±0.3 ML. Then, we secured the device to the skull with tissue glue and sutured the skin.

Behavioral Assays. For the home cage arousal experiments, we performed all behavioral experiments in a sound-attenuated room maintained at 23 °C at least 1 wk following the final surgery. At 10:00 AM, during a period of normal sleep and less activity, we recorded the activity of the mice for three successive 15-min periods by using Ethovision 8.5 (Noldus Information Technologies, RRID: rid_000100). During the first and last period, there was no activation of the implantable system. During the second period, the implanted system illuminated the LC under stimulation conditions (10 Hz, 50 ms pulse widths), which were previously shown to drive LC activation by ChR2 (14, 30).

For multichannel control of neuronal subpopulation experiments, we placed mice in a custom-made unbiased, balanced two-compartment conditioning apparatus ($52.5 \times 25.5 \times 25.5$ cm³) as described previously (12). During a 20-min trial, entry into one compartment led to activation of the devices and provided photostimulation to the NAcSh (rf-on) (10 Hz, 50 ms pulse widths), whereas the animal remained in the light-paired chamber and entry into the other chamber ended photostimulation (rf-off). Arrangement of the transmitting antennas targeting only one side of the real-time place preference assay led to the unilateral rf transmission. With this configuration, the active side of the assay always received rf transmission (rf-on). The rf signal generator power output ranged from –10 to 0 dBm at 2.3, 2.5, and 2.7 GHz for each LED device.

Statistics/Data Analysis. We showed all grouped data as mean ± SEM. Data were normally distributed, and independent Student's two-tailed, unpaired or paired, t tests determined differences between two groups. One-way or two-way analysis of variances (ANOVAs) followed by post hoc Bonferroni or Dunnett's multiple comparisons, if the main effect was significant at $P < 0.05$, determined differences between multiple groups. We took statistical significance as $*P < 0.05$, $**P < 0.01$, $***P < 0.001$, $****P < 0.0001$ and conducted all analyses using Prism 5.0 (GraphPad).

1. Boyden ES, Zhang F, Bamberg E, Nagel G, Deisseroth K (2005) Millisecond-timescale, genetically targeted optical control of neural activity. *Nat Neurosci* 8(9):1263–1268.

2. Adamantidis AR, Zhang F, Aravanis AM, Deisseroth K, de Lecea L (2007) Neural substrates of awakening probed with optogenetic control of hypocretin neurons. *Nature* 450(7168):420–424.

3. Berndt A, Lee SY, Ramakrishnan C, Deisseroth K (2014) Structure-guided transformation of channelrhodopsin into a light-activated chloride channel. *Science* 344(6182):420–424.

4. Park S-I, et al. (2015) Ultraminiaturized photovoltaic and radio frequency powered optoelectronic systems for wireless optogenetics. *J Neural Eng* 12(5):056002.

5. Deisseroth K (2014) Circuit dynamics of adaptive and maladaptive behaviour. *Nature* 505(7483):309–317.

6. Paralikar K, et al. (2011) An implantable optical stimulation delivery system for actuating an excitable biosubstrate. *IEEE JSSC* 46:321–332.

7. Park S-I, et al. (2015) Soft, stretchable, fully implantable miniaturized optoelectronic systems for wireless optogenetics. *Nat Biotechnol* 33(12):1280–1286.

8. Montgomery KL, et al. (2015) Wirelessly powered, fully internal optogenetics for brain, spinal and peripheral circuits in mice. *Nat Methods* 12(10):969–974.

9. Kim TI, et al. (2013) Injectable, cellular-scale optoelectronics with applications for wireless optogenetics. *Science* 340(6129):211–216.

10. McCall JG, et al. (2013) Fabrication and application of flexible, multimodal light-emitting devices for wireless optogenetics. *Nat Protoc* 8(12):2413–2428.

11. Siuda ER, et al. (2015) Optodynamic simulation of β-adrenergic receptor signaling. *Nat Commun* 6:8480.

12. Al-Hasani R, et al. (2015) Distinct subpopulations of nucleus accumbens dynorphin neurons drive aversion and reward. *Neuron* 87(5):1063–1077.

13. Iyer SM, et al. (2014) Virally mediated optogenetic excitation and inhibition of pain in freely moving nontransgenic mice. *Nat Biotechnol* 32(3):274–278.

14. Carter ME, et al. (2010) Tuning arousal with optogenetic modulation of locus coeruleus neurons. *Nat Neurosci* 13(12):1526–1533.

15. Kittel C, Kroemer H (1980) *Thermal Physics* (W.H. Freeman, New York), 2nd Ed.

16. Kim D-H, et al. (2011) Epidermal electronics. *Science* 333(6044):838–843.

17. Hwang S-W, et al. (2012) A physically transient form of silicon electronics. *Science* 337(6102):1640–1644.

18. Tao H, et al. (2014) Silk-based resorbable electronic devices for remotely controlled therapy and in vivo infection abatement. *Proc Natl Acad Sci USA* 111(49):17385–17389.

19. Hwang S-W, et al. (2014) 25th anniversary article: Materials for high-performance biodegradable semiconductor devices. *Adv Mater* 26(13):1992–2000.

20. Balanis CA (2005) *Antenna Theory Analysis and Design* (Wiley-Interscience, Hoboken, NJ), 3rd Ed.

21. Matteis J, et al. (2012) Principles for applying optogenetics tools derived from direct comparative analysis of microbial opsins. *Nat Methods* 9:159–172.

22. Gradinaru V, et al. (2007) Targeting and readout strategies for fast optical neural control in vitro and in vivo. *J Neurosci* 27(52):14231–14238.

23. Hashimoto M, Hata A, Miyata T, Hirase H (2014) Programmable wireless light-emitting diode stimulator for chronic stimulation of optogenetic molecules in freely moving mice. *Neurophotonics* 1(1):011002.

24. Wentz CT, et al. (2011) A wirelessly powered and controlled device for optical neural control of freely-behaving animals. *J Neural Eng* 8(4):046021.

25. Park S-I (2013) Enhancement of wireless power transmission into biological tissues using a high surface impedance ground plane. *Prog Electromagnetics Res* 135:123–136.

26. Peyman A, Rezazadeh AA, Gabriel C (2001) Changes in the dielectric properties of rat tissue as a function of age at microwave frequencies. *Phys Med Biol* 46(6):1617–1629.

27. Adiv G (1985) Determining three-dimensional motion and structure from optical flow generated by several moving objects. *IEEE Trans Pattern Anal Mach Intell* 7(4):384–401.

28. Vazey EM, Aston-Jones G (2014) Designer receptor manipulations reveal a role of the locus coeruleus noradrenergic system in isoflurane general anesthesia. *Proc Natl Acad Sci USA* 111(10):3859–3864.

29. Holets VR, Hökfelt T, Rökaeus A, Terenius L, Goldstein M (1988) Locus coeruleus neurons in the rat containing neuropeptide Y, tyrosine hydroxylase or galanin and their efferent projections to the spinal cord, cerebral cortex and hypothalamus. *Neuroscience* 24(3):893–906.

30. McCall JG, et al. (2015) CRH engagement of the locus coeruleus noradrenergic system mediates stress-induced anxiety. *Neuron* 87(3):605–620.

31. Siuda ER, et al. (2015) Spatiotemporal control of opioid signaling and behavior. *Neuron* 86(4):923–935.

32. Jeong J-W, et al. (2015) Wireless optofluidic systems for programmable in vivo pharmacology and optogenetics. *Cell* 162(3):662–674.

33. Gong S, et al. (2003) A gene expression atlas of the central nervous system based on bacterial artificial chromosomes. *Nature* 425(6961):917–925.

34. Wu Z, Autry AE, Bergan JF, Watabe-Uchida M, Dulac CG (2014) Galanin neurons in the medial preoptic area govern parental behaviour. *Nature* 509(7500):325–330.

Supporting Information

Park et al. 10.1073/pnas.1611769113
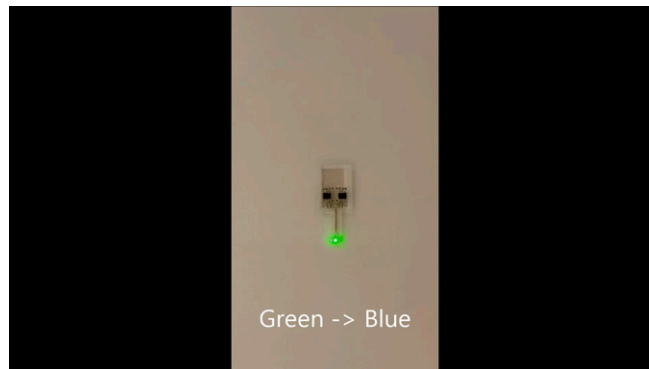
Movie S1. Video of an operating device. These results demonstrate that the frequency of the incident rf radiation can be adjusted to activate separate LEDs independently.

[Movie S1](#)

Movie S2. Video of a freely behaving animal with an implanted device located to allow visual examination of operation. These results demonstrate that wireless power transmission systems can enable continuous operation throughout a location of interest.

[Movie S2](#)

Other Supporting Information Files

[SI Appendix (PDF)](#)

Supplementary Note 1: Arrhenius model

To assess chronic reliability, we utilized extrapolations based on Arrhenius scaling of time to failure with temperature. By observing the behavior of devices at elevated temperatures, this scaling approach yields estimates for the time of failure at reduced temperatures. This form of accelerated testing utilizes the Arrhenius equation:

$$r = A \exp(\frac{-E_a}{kT}) \tag{1}$$

where r = rate of the process, A = a proportional multiplier, E_a = the activation energy for the process, and k = Boltzmann constant.

Rearranging the equation yields a model for the temperature dependence of the failure time,

$$\ln\left(\frac{t_2}{t_1}\right) = \frac{E_a}{k}\left(\frac{1}{T_2} - \frac{1}{T_1}\right) \tag{2}$$

where t_1 = time to failure at T_1 and t_2 = time to failure at T_2.

For T_1 = 90 °C, T_2 = 60 °C, experiments show that t_1 = 6 days and t_1 = 30 days. From these data, the value of E_a can be determined to be 60 kJ/(mol.K), similar to values in the literature [1]. This information allows extrapolation to time to failure at 37 °C, which is 180 days (6 months).

Supplementary Note 2: Tailored properties in stretchable multi-channel antennas

Stretchable multi-channel antennas can be designed with a wide range of operating frequencies. **Supplementary Fig. 5** explains the process of selecting designs that define a desired pair of operational frequency (and, therefore, channel separation). In these examples, the operation frequency at Channel 2 varies from 2.7 to 3.1 GHz with a frequency of 2.3 GHz at Channel 1. The total capacitance required for resonance at the corresponding frequency ranges appears in **Supplementary Fig. 5**. This capacitance provides an estimate of the dimensions of the antenna. Based on the estimates and unit capacitances in **Fig. 4D**, it is possible to determine the number of serpentine pairs needed for resonance at the operation frequency.

Supplementary Note 3: Calculation of electrostatic potential and capacitance

Assume that the length in the X-direction is much greater than the height in the Y-direction. The boundary function of the serpentine lines can be expressed by,

$$y = h - l\cos(kx) \quad \text{where } k = \frac{2\pi}{p} \tag{3}$$

The electrostatic potential function, $\Psi(x, y)$, satisfies the boundary and periodic conditions given by,

$$\Psi(x, y) = \begin{cases} V_0 & \text{if } y = h - l\cos(kx) \\ -V_0 & \text{if } y = -h + l\cos(kx) \end{cases} \tag{4}$$

$$\Psi(x, y) = \Psi(x + p, y) \tag{5}$$

Based on these conditions, one can solve Laplace equation,

$$\frac{\delta^2 \Psi(x,y)}{\delta x^2} + \frac{\delta^2 \Psi(x,y)}{\delta y^2} = 0 \tag{6}$$

beginning with a general solution that exploits separation of variables.

$$\Psi(x, y) = X(x)Y(y) \tag{7}$$

Plugging the (7) into (6) and imposing the conditions in (4) and (5) leads to

$$X_n(x) = a_n\cos(nkx) + b_n\sin(nkx) \quad n = 1,2,3,\dots \tag{8}$$

$$Y_n(y) = c_n e^{nky} + d_n e^{-nky} \quad n = 1,2,3,\dots \tag{9}$$

$$a\cos(qx) + b\sin(qx) = a\cos(q(x + p)) + b\sin(q(x + p))$$

$$\text{where } q, p = 2\pi n, \ n = 1,2,3,\dots \tag{10}$$

$$\Psi_n(x, y) = \left(a_n\cos(nkx) + b_n\sin(nkx)\right)\left[c_n e^{nky} + d_n e^{-nky}\right],$$

$$n = 1,2,3,\dots \tag{11}$$

$$\Psi(x, y) = \frac{V_0}{h} y + \frac{V_0}{h} \frac{sinh(ky)\,cos(kx)}{sinh(k(h-l\,cos(kx)))} \qquad k = \frac{2\pi}{p} \qquad (12)$$

The derivative of this expression with respect to y yields the Y components of the electric field,

$$\mathrm{E}_Y(x, y) = -\frac{V_0}{h} - \frac{V_0}{h} k \frac{cosh(ky)\,cos(kx)}{sinh(k(h-l\,cos(kx)))} \qquad k = \frac{2\pi}{p} \qquad (13)$$

Next, we calculate the capacitance between two serpentine lines. This serpentine shaped- capacitor consists of infinite capacitors where capacitance is determined by (**Fig. 4B**),

$$dC = \varepsilon \frac{dx}{y} \qquad \text{where } y = 2h + 2\,l\,sin\,x \qquad (14)$$

Integrating this expression along the length of the serpentine lines yields the capacitance.

$$C = \int dC = \int \frac{dx}{y} = \int \frac{dx}{2h + 2\,l\,sin\,x} \qquad (15)$$

Supplementary Note 4: MATLAB code for motion tracking algorithm

```
vidDevice = imaq.VideoDevice('winvideo', 1, 'YUY2_320x240', ...
'ROI', [1 1 320 240], ...
'ReturnedColorSpace', 'rgb');
optical = vision.OpticalFlow('OutputValue', 'Horizontal and vertical components in complex form');
maxWidth = imaqhwinfo(vidDevice,'MaxWidth');
maxHeight = imaqhwinfo(vidDevice,'MaxHeight');
shapes = vision.ShapeInserter;
shapes.Shape = 'Lines';
shapes.BorderColor = 'Custom';
shapes.CustomBorderColor = [255 0 0];
r = 1:20:maxHeight;
c = 1:20:maxWidth;
[Y, X] = meshgrid(c,r);
hVideoIn = vision.VideoPlayer;
hVideoIn.Name = 'Original Video';
hVideoIn.Position = [30 100 320 240];
hVideoOut = vision.VideoPlayer;
hVideoOut.Name = 'Motion Detected Video';
hVideoOut.Position = [400 100 320 240];
nFrames = 0;
```

```matlab
devices = daq.getDevices;
devices(1);
s = daq.createSession('ni');
addDigitalChannel(s,'Dev1','port0/line0:3','OutputOnly');
outputSingleScan(s,[ 1 1 1 1]);
sum=0;
while (nFrames < 2000)
rgbData = step(vidDevice);
optFlow = step(optical,rgb2gray(rgbData));
optFlow_DS = optFlow(r, c);
H = imag(optFlow_DS)*50;
V = real(optFlow_DS)*50;
lines = [Y(:)'; X(:)'; Y(:)'+V(:)'; X(:)'+H(:)'];
rgb_Out = step(shapes, rgbData, lines');
%%rgb_Out = step(shapes, rgb_Out, lines');
%%step(hVideoIn, rgbData);
step(hVideoOut, rgb_Out);
x=rgbData-rgb_Out;
for i=1:1:240
    for j=1:1:320
        if (x(i,j,3) > 0)
            if (j >160)
            outputSingleScan(s,[ 0 0 0 0]);
                i=240;
                        j=320;
            else
              outputSingleScan(s,[ 1 1 1 1]);
                i=240;
        j=320;
            end
        end
    end
end

nFrames = nFrames + 1;
end
release(hVideoOut);
release(hVideoIn);
release(vidDevice);
```

Reference

1. Thomas, T. H. & Kendrick, T.C. Thermal Analysis of Polydimethylsiloxanes. I. Thermal

   Degradation in Controlled Atmospheres. *J.Polym. Sci*. 7, 537-549 (1969).
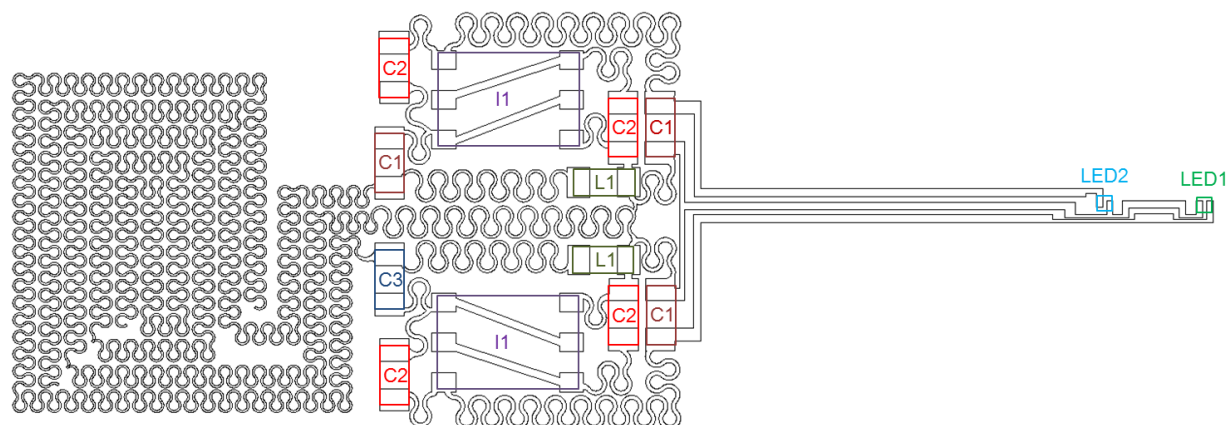
	Components	Product number	Vendor information
LED1	540 nm, 0.22 mm x 0.27 mm x 0.05 mm	C527TR2227-0215	Cree Inc.
LED2	465 nm, 0.22 mm x 0.27 mm x 0.05 mm	C460TR2227-0216	Cree Inc.
C1	Capacitor, 1 pF, 0.2 mm x 0.4 mm x 0.22 mm	250R05L1R0BV4T	Johanson Technology
C2	Capacitor, 5 pF, 0.6 mm x 0.3 mm x 0.33 mm	250R05L5R1CV4T	Johanson Technology
C3	Capacitor, 3 pF, 0.6 mm x 0.3 mm x 0.33 mm	250R05L3R1CV4T	Johanson Technology
I1	Schottky diode, 1.7 mm x 1.5 mm x 0.5 mm	1PS66SB82,115	NXP Semiconductor
L1	Inductor, 2.7 nH, 0.2 mm x 0.4 mm x 0.22 mm	L-05B2N7SV6T	Johanson Technology

Supplementary Fig. 1. Layout and component information for the multi-channel devices.
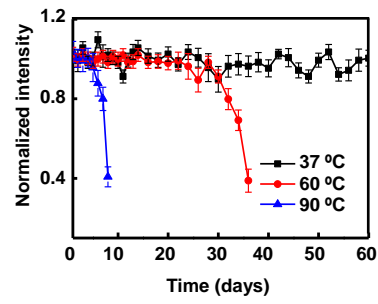
Supplementary Fig. 2. Assessment of variations in normalized light intensity produced by the multi-channel system as a function of time of immersion in physiological PBS (7.4 pH) solution at three different temperatures.
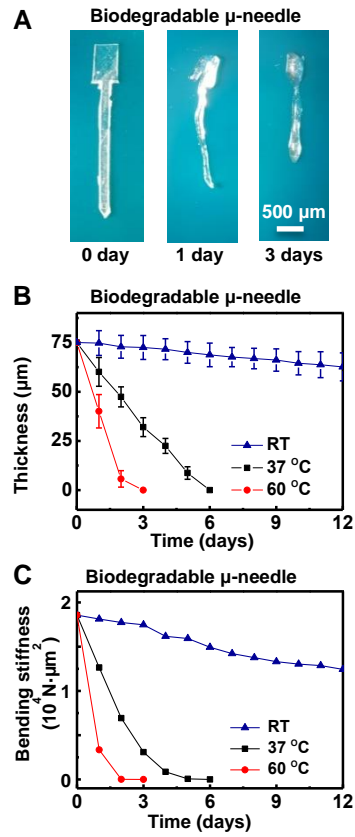
Supplementary Fig. 3. (A) Images of a biodegradable, injectable μ-needle in physiological PBS solution after 0 day (left), 1 day (middle), and 3 days (right) respectively. Results of measurements of the μ-needle thickness (B) and bending stiffness (C) as a function of time of immersion in PBS at a variety of temperatures.
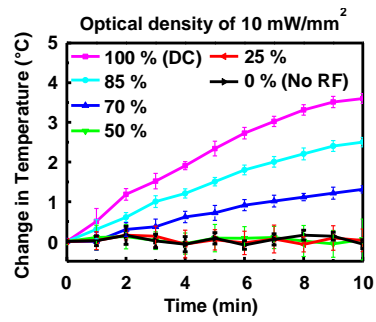
Supplementary Fig. 4. In vivo monitoring of temperature of a mouse during device operation, for various duty cycles (DC).
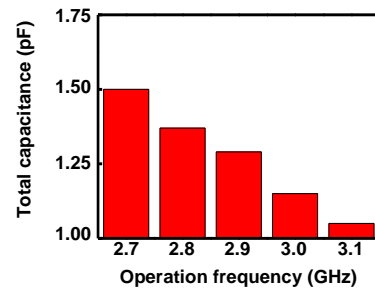
Supplementary Fig. 5. Total capacitance values for stretchable antennas with resonance frequencies between 2.7 to 3.1 GHz .
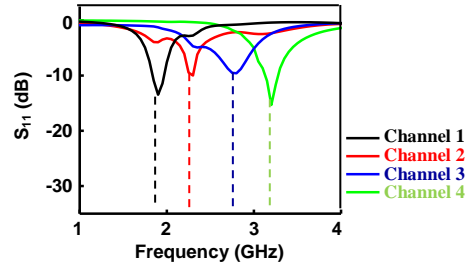
Supplementary Fig. 6. Scattering coefficients, S_{11}, of a 4-channel stretchable antenna. The antenna has 4 operation channels at a frequency of 1.9 (black), 2.2 (red), 2.8 (blue), and 3.2 (green) GHz, respectively.
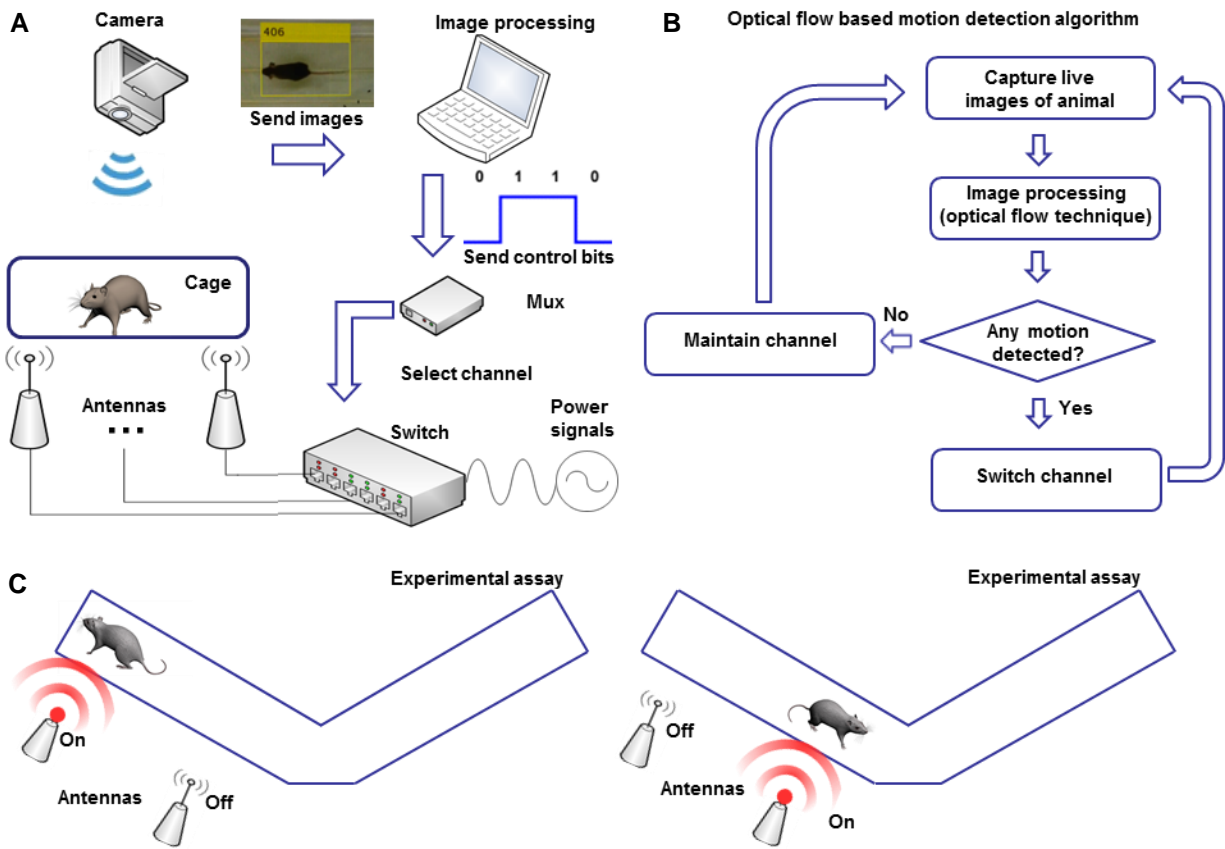
Supplementary Fig. 7. (A) Illustration of motion tracking power transmission systems. A camera monitors the location of a mouse and sends images to the base station, which processes the images and sends control signals to the multiplexer (Mux). Output signals from Mux manipulate a switch that activates the appropriate circuit to transmit power with the appropriate antenna. These processes occur within 1 ms which is fast enough to respond to the motions of a mouse instantaneously. (B) Flowchart of the motion detection algorithm. (C) Illustration of smart power transmission. The antenna that is closest to the mouse is enabled and transmits power.
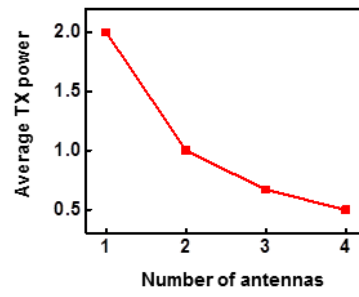
Supplementary Fig. 8. Plot of average TX power as a function of number of antennas. The smart power system distributes a given TX power of 2 W across the antennas.
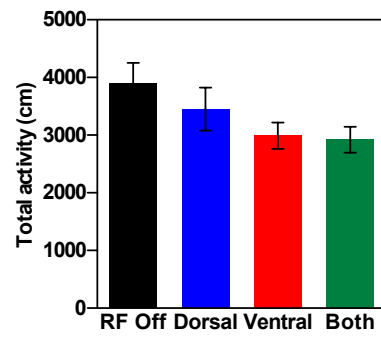
Supplementary Fig. 9. Analysis of the total distance traveled, as an assessment of activity level, during a 20 min experiment.

Process	Purpose	Required time for 5 devices	Equipment	Progress level (%)
1. Preparation of PMMA coated glass	Sampling for transfer	0.5 hour	Cleanroom Spin-coater	5
2. PI film fabrication	Bottom encapsulating layer	1.5 hours	Cleanroom, Vacuum oven	15
3. Metal (Ti/Au) deposition	Interconnection	1.5 hours	E-beam deposition	25
4. Metal patterning		1 hours	Cleanroom, Mask aligner	30
5. PI encapsulation	Top encapsulating layer	1.5 hours	Cleanroom, Vacuum oven	40
6. PI/Metal/PI patterning	Patterning for stretchable circuits	1 hours	Cleanroom, mask aligner,	50
7. PI etching		1.5 hours	RIE	60
6. Components transfer	Active components integration	2.5 hours	Solder, Microscope	80
7. PDMS encapsulation	System packaging	0.5 hour	Oven	100

Supplementary Table 1: Fabrication process details

Supplementary Movie 1. Video of an operating device. This demonstrates that the frequency of the incident RF radiation can be adjusted to activate the channels independently.

Supplementary Movie 2. Video of a freely behaving animal with the device implanted in a cage. This demonstrates that wireless power transmission systems can enable continuous operation throughout a location of interest.